Supporting Information for: "The Impact of Plate Motions on Long-Wavelength InSAR-Derived Velocity Fields"

Oliver L. Stephenson[*1], Yuan-Kai Liu[*+1], Zhang Yunjun[1], Mark Simons[1],

Paul Rosen[2], and Xiaohua Xu[3]

[1]Seismological Laboratory, Division of Geological and Planetary Sciences,

California Institute of Technology, Pasadena, CA 91125, USA.

[2]Jet Propulsion Laboratory, California Institute of Technology, Pasadena, CA 91109, USA.

[3]Institute for Geophysics, University of Texas at Austin, Austin, TX 78758, USA.

[*]Contributed equally

[+]Corresponding author

Contents of this File

1. Text S1 to S4

2. Table S1 to S3

3. Figure S1 to S8

―――――――

October 9, 2022, 7:17pm

Introduction

Here, we present more details on the SAR data sources (Table S1) and processing steps (Text S1). In Text S2 we give further details on the corrections that we apply to our data and the possible sources of residual signals after these corrections are applied. In Figures S1-S5 we present the velocity corrections for all tracks other than Makran track 86, which is shown in the main text (Figure 2). In Text S3 we provide further information on how rigid vertical and horizontal motions impact InSAR velocity fields, and in Figure S6 we present a figure that can be used to estimate the scale of velocity ramp for ascending (ASC) and descending (DSC) tracks for a given plate velocity. In the Discussion, we stated that plate motion could bias calculations of 3D velocities from multiple overlapping InSAR tracks, which we illustrate in Text S4 and Figure 4. In Figures S8-S10, we demonstrate the comparison between plate motion model correction with pure empirical deramping in tracks of Makran and the Gulf of Aqaba. Table S2-S3 and Figure S7 report the spatial standard deviation (σ mm/yr) of each correction stage, which we reference in Section 2 and Figure 2 of the Main text, and Figures S1-S5.

October 9, 2022, 7:17pm

Text S1: InSAR Processing Details

We download Sentinel-1 Single Look Complex (SLC) data from the Alaska Satellite Facility. We process our data using the InSAR Scientific Computing Environment (ISCE-2, Rosen et al. (2012), and see `https://github.com/isce-framework/isce2`). For the Makran data (tracks 86 and 20), we use the `ISCE-2/topsApp` processing chain, where each interferometric pair is processed separately. Other tracks are processed using `ISCE-2/topsStack`, which coregisters all SLCs to a single reference image at the start of the processing. `topsStack` therefore avoids the need to repeat the coregistration for every interferometric pair, reducing computational expense compared to `topsApp`.

Each acquisition is used to form interferograms with the next three SLCs. We use satellite orbits from the Copernicus Precise Orbit Determination service and digital elevation models from the Shuttle Radar Topography Mission to remove the phase contribution from the viewing geometry. To correct for azimuth misregistration we apply enhanced spectral diversity (ESD) (De Zan et al., 2014) for each pair. When processing data using `topsStack`, we estimate azimuth misregistration for each date in a network sense based on ESD results for each pair (Fattahi, Agram, & Simons, 2017), but do not use the network approach for `topsApp`. The different approaches are unlikely to have a significantly different impact on the long-wavelength velocity field from long time series. Two-dimensional phase unwrapping is performed using the SNAPHU algorithm for each interferogram (Chen & Zebker, 2002).

We use the range split-spectrum method of Liang et al. (2019) to estimate the ionospheric phase screen in each interferogram. For `topsStack` data, the ionospheric phase

October 9, 2022, 7:17pm

is estimated for each interferogram, then for each date by network inversion (Fattahi, Simons, & Agram, 2017). The ionosphere correction is then applied in the time series domain. For `topsApp` data, the ionospheric phase screen is estimated and removed before the final phase unwrapping. As long as we remove interferograms where there are clear unwrapping errors in the ionosphere, we expect the difference between these approaches to be insignificant.

We calculate InSAR time series from the interferometric network using the SBAS methodology (Berardino et al., 2002), implemented in `MintPy` (Yunjun et al., 2019). The secular velocity is obtained from a linear, least-squares fit to the time series. We use the `PyAPS` software package to apply corrections for the troposphere with ERA-5 weather models (Jolivet et al., 2011, 2014). Solid Earth tides removal is performed using `PySolid` (Milbert, 2018; Yunjun et al., 2022), and the Digital Elevation Model (DEM) error is estimated from the correlation between the residual time series and perpendicular baseline, as described in Fattahi and Amelung (2013). All of the above corrections are applied to the deformation time series. We apply the plate motion adjustment in the velocity domain. As we are performing linear least-squares fits to the time series, the plate motion correction could be straightforwardly applied to the time series (assuming a constant plate rate over time) with identical results (as shown in the bottom time series in Figure 2l). All other corrections could similarly be applied either in the velocity domain or the time series domain and result in the same final velocity, assuming we obtain the velocities from a linear fit to the time series.

For the Makran and Aqaba datasets we mask out unreliable data based on the union of connected component masks from every interferogram (i.e., areas identified as unreliably unwrapped by the SNAPHU algorithm (Chen & Zebker, 2002)). This is a conservative approach to masking that removes a large amount of the data, but allows us to focus on long-wavelength features. The lower coherence for our Australian tracks means that the connected component mask removes too much data to view the spatial velocity pattern, so we instead mask out points with an average spatial coherence below 0.82. This less conservative masking strategy leads us to include noisier data, possibly biasing our estimation of the across track ramp.

Text S2: Further Details on InSAR Corrections and Residuals

To illustrate the influence of the corrections on the final secular velocity, we perform a linear, least-squares fit to the time series of each of the applied corrections (these fits are shown in the second row of Figures 2 and S1-S5). While we fit a linear velocity term for the figures to show how the corrections affect the measured secular velocity, we do not expect these corrections to have a linear variation in time. As these corrections are not perfect, and we have not accounted for all potential contributors to our velocity fields, we also need to consider what other residuals may remain in our time series. Of particular interest is the extent to which the velocity ramps before plate motion correction can be attributed to sources other than plate motion. Below, we present more details on these corrections and the residuals that may remain in our data.

The strength of ionospheric signals is controlled by the density of charged particles in the ionosphere (Gomba et al., 2016). Ionization is mainly due to solar radiation, meaning the

ionospheric signal depends on factors such as the time of day, the geomagnetic latitude, and the approximately 11-year solar cycle (Liang et al., 2019). Sentinel-1 ascending tracks are acquired at dusk (around 6 pm local solar time), and suffer from much stronger ionospheric impacts than the Sentinel-1 descending tracks which are acquired at dawn (around 6 am local solar time). The most recent peak of solar activity occurred in April 2014, decreasing to a minimum in December 2019, meaning that data earlier in our time series (which start in late 2014 for Aqaba and Makran) have much stronger ionospheric effects than later dates. This long-term variation in the ionosphere means that we cannot average out the ionospheric signal by fitting to several years of data, making the ionosphere the most significant correction to the secular velocity for the ascending tracks we study.

Ionospheric corrections substantially reduce long-wavelength velocity ramps for the ascending tracks we present here, but it is hard to quantify what residual ionospheric signals may be left without comparing to external data. Liang et al. (2018) compared the long-wavelength signal with GNSS velocities after ionosphere correction using the split-spectrum method. They found good agreement between the long-wavelength InSAR and GNSS velocities, suggesting that residual ionosphere was not having a significant impact on the long-wavelength InSAR signals after correction.

Errors in the ionosphere estimation can be introduced by unwrapping errors in the sub-band interferograms (Gomba et al., 2016; Liang et al., 2019) and before time series processing we examine the ionospheric phase estimates and remove those that have obvious unwrapping errors. Unwrapping the sub-band interferograms requires strong filtering (Liang et al., 2019), meaning that the split-spectrum method is not able to capture short-

wavelength variations in the ionospheric signal. We observe the strength of the calculated long-wavelength ionospheric signal to vary with solar activity, which declined from a peak in April 2014 to a minimum in December 2019, and we would expect the short wavelength ionosphere to follow the same pattern. If we have a substantial component of short wavelength ionospheric noise, this might then show up as larger residuals in the time series for the earlier dates (2014-15) compared to dates in late 2019. To test this, we first fit and remove from every pixel a functional form (a linear term plus the amplitude and phase of annual and semi-annual sinusoids), then calculate the root mean square (RMS) of the residuals for every acquisition. The primary variation in the residual RMS is seasonal (e.g., varying between about 10 mm and 45 mm for track 86 (ASC) in the Makran), likely due to incompletely removed tropospheric delays. There is not a strong trend in the RMS over longer timescales, suggesting the short wavelength ionosphere remaining in our data is not having a substantial effect, particularly compared with residual troposphere.

The geometry of the Sentinel-1 bursts can result in ionospheric phase discontinuities at the burst boundaries (see Section III.C in Liang et al. (2019)). The topsApp code is able to compute and remove these discontinuities as part of the ionosphere estimation. The removal of burst discontinuities due to the ionosphere can be most clearly seen in the ladder-like pattern of the velocity in Figure S1(f), which is the calculated ionospheric signal removed from S1(a). Here, the ionosphere is contributing ramps of up to 0.5 mm/yr over the 20 km along-track width of the bursts, with sharp discontinuities of up to 0.5 mm/yr at the burst boundaries. These ramps and discontinuities are removed by the ionosphere correction. The burst ramps and discontinuities are also present in

the ionosphere estimation of the ascending track (Figure 2(f)), which is also performed using topsApp, but cannot be seen in the figure due to the wider dynamic range of the long-wavelength ionospheric gradient in the ascending observation geometry.

The `topsStack` code is not yet able to take account of the burst geometry when computing the ionospheric phase screen. For the tracks processed using topsStack (Aqaba and Australia), the lack of accounting for the burst geometry results in small discontinuities in the velocity field at the burst boundaries in the final velocity field, which can be seen on close inspection of Figures S2-S5. Nevertheless, the phase ramp is zero-mean in space for each burst and are below the 1 mm/yr level, and are short-wavelength ramps within the bursts, meaning they do not affect the long-wavelength velocity field.

If there are errors in the long-wavelength ionospheric phase removal, and these errors are proportional to the size of the ionospheric signal, they could be revealed by differences in the long-wavelength residual velocity field between ascending and descending tracks covering the same region. For both Makran and Aqaba, there do not seem to be substantial differences in the long-wavelength residuals between the ascending and descending tracks that could reasonably be attributed to uncompensated ionosphere. These results suggest that the ionosphere corrections are able to remove a substantial fraction of the long-wavelength ionospheric signal, but we are not able to precisely quantify the residual long-wavelength ionosphere.

Unlike ionospheric signals, the tropospheric phase is dominated by seasonal variability, meaning longer time series will reduce the tropospheric effect on the estimated secular velocity (Fattahi & Amelung, 2015; Parizzi et al., 2021). The troposphere signal varies

October 9, 2022, 7:17pm

depending on the location, but can have an amplitude equivalent to tens of centimeters of ground deformation. This signal can be mitigated, but not eliminated, by tropospheric models (Fattahi & Amelung, 2015; Bekaert et al., 2015; Parizzi et al., 2021). Fattahi and Amelung (2015) examined the tropospheric noise just to the west of the Makran subduction zone, finding that, after corrections with the ERA-Interim weather model, the tropospheric delay would lead to uncertainties in the InSAR-derived velocities of 2 mm/yr over 100km and 4 mm/yr over 400km with 7 years of Envisat data. Parizzi et al. (2021) evaluated the tropospheric contribution to InSAR-derived velocity uncertainties for locations at global scales including the Markan and Gulf of Aqaba. They estimated that uncertainties were in the range 2-4 mm/yr over 150 km for the Makran, and 1-2 mm/yr over 150 km in the Gulf of Aqaba, using at least four years of Sentinel-1 data and corrections from the ERA5 weather model from ECMWF. They stated that tropospheric signals are the limiting factor for measuring large-scale deformation using InSAR, as the residuals from the ionosphere and solid Earth tides are negligible after correction, and the contribution of orbital errors is also not significant compared with the troposphere.

Our data spans 5-7 years, with 150-200 acquisitions per track (Table S1), and we use the ERA5 weather model in our corrections (Hersbach et al., 2020). We therefore expect the contribution of the troposphere to the velocity field to be at or below the levels outlined by Parizzi et al. (2021) for Makran and Aqaba, but we have not directly estimated this for our data. We also do not have comparable estimates for the Australian tracks.

Tracks in the same region acquired at the same time of day should have statistically similar tropospheric signals in terms of the amplitude and spatial correlation of the phase in

each acquisition. Tropospheric signals can therefore create similar InSAR velocity uncertainties for nearby tracks (e.g., Fattahi and Amelung (2015)). However, the troposphere is uncorrelated at timescales longer than a day (Emardson et al., 2003), meaning tracks in the same region whose acquisitions are separated by more than a day (as is the case for all of our tracks in the same region) will have different realisations of the tropospheric phase in each acquisition. We would therefore expect the long-wavelength velocity residuals from the troposphere to be different for each track in a given region, rather than systematically contributing velocity ramps in a particular direction. This expectation also applies to tropospheric residuals that remain after troposphere corrections have been applied.

Orbital errors can also create long-wavelength artefacts in individual interferograms, which can impact the velocity estimate. Fattahi and Amelung (2014) found that for Sentinel-1, orbital errors would lead to velocity uncertainties at the level of 0.5 mm/yr over 100 km, assuming 15 acquisitions per year for 8 years. Similarly to the troposphere, we would expect the orbital error to have different realisations in each track, meaning that the velocity ramps from orbital errors would not be expected to occur systematically in any particular direction.

The solid Earth tides (SET) are another long-wavelength signal. SET can contribute along-track InSAR phase ramps, and the varying satellite line-of-sight (LOS) will also mean that SET deformation creates ramps in the range direction as well (Xu & Sandwell, 2020), in a similar fashion to the LOS projection of plate motion. The SET are periodic, and the Sentinel-1 sampling frequency causes diurnal and semi-diurnal tidal periods to be

aliased to longer periods of up to a year (Xu & Sandwell, 2020). Using multi-year time series reduces the influence of these periodic terms on the secular velocity estimation. The SET estimate is accurate to better than 1 mm (Petit & Luzum, 2010), so after correction we expect its residual contribution to the long-wavelength velocity to be much smaller than other signals discussed here.

We do not correct for the deformation due to ocean tidal loading (OTL) in this work (Dicaprio et al., 2008). OTL is a periodic, long-wavelength signal, much like the SET, and the satellite LOS variation causes changing sensitivity to this deformation in the range direction. The periodic nature of the signal means that it will cause a smaller bias in the estimated secular velocity in longer time series (Yu et al., 2020), similarly to the SET. We expect deformation due to OTL to decay with distance from the ocean, meaning the direction and magnitude of any long-wavelength velocity residuals due to OTL will be different for each of our regions. Yu et al. (2020) identified regions of the Earth where OTL corrections would be significant for reducing long-wavelength residuals (see Figure 1 in Yu et al. (2020)). As all of our study areas lie outside these regions, we believe that the OTL signal will have a smaller influence on the velocity than corrections such as the ionosphere, troposphere and plate motion, but may be comparable to the SET, particularly for the Makran.

The DEM error signal is generally short wavelength, as well as depending on the satellite baseline (Fattahi & Amelung, 2013), which is well controlled for Sentinel-1 (Li et al., 2016) and varies largely randomly in time. The DEM error signal is estimated from correlation between the perpendicular baseline and time series residuals, meaning that large residuals

from other sources, such as the troposphere, can potentially bias the DEM error estimation (Fattahi & Amelung, 2013). It is possible that we see this biasing in Figure 2(i) at around (26°N, 60°E), but the impact is still small, at around 0.5 mm/yr over 100 km. Even with the biasing from residual troposphere, we expect residual long-wavelength noise from DEM error to be well below residuals from other sources after correction.

Decorrelation is an additional source of noise in InSAR measurements (Zebker & Villasenor, 1992). Changes in the surface properties can alter the interferometric phase, which causes noise in the estimates of the deformation time series and thus greater errors in the calculated secular velocity. We do not expect this noise source to vary systematically over long distances, so it is unlikely to create significant biases in the long-wavelength velocity field. The impact of decorrelation can be seen by comparing tracks from Australia and the Makran. Lower coherence of the Australian interferograms compared with the Makran causes the Australian track velocity profiles to have a larger scatter in the velocities (Figure 3).

Another source of noise comes from the closure phase introduced as a result of multi-looking combined with phase-changing physical processes on the Earth's surface (Ansari et al., 2021; Zheng et al., 2022). While this can bias velocity estimates, we would not expect to see systematic spatial biases in the velocity over hundreds of kilometers, so we do not expect this signal to contribute substantially to the long-wavelength velocity field.

Even when a term does not contribute to the long-wavelength velocity field (say, varying on a scale of well under 100 km), it can still bias the estimate of the across track ramp, with the bias being more pronounced for shorter tracks. It is possible that this explains

the larger residual across track ramp for track 46 (Australia). This track is the shortest in our data set, and also has the largest across track residual after plate motion correction, at 1.5 mm/yr/track. For longer tracks, the bias on the ramp estimation by short-wavelength terms is reduced. This reduction in bias is similar to longer time series having a secular velocity that is less biased by periodic terms.

The expected amplitude and spatial wavelength of the residuals discussed above, as well as the consistency between multiple tracks, including ascending and descending tracks covering the same area, gives additional credence to the claim that the long-wavelength range-dependent ramps that we observe in our data after applying corrections are primarily due to plate motion. Plate motion and ionosphere are the two signals that have secular trends over several years, whereas signals such as the troposphere and SET are dominated by seasonal variations. It is this temporal variation that explains why the ionosphere and plate motion are dominant contributors to the long-wavelength velocities in our multi-year time series, while the large amplitude of troposphere variation results in it also contributing substantially.

Text S3: Further Details on the Signal of Vertical and Horizontal Plate Motions in InSAR Measurements

In Figure S6, we show estimates of the scale of the velocity ramp in the satellite range direction for given vertical or horizontal plate translation. The values are calculated by subtracting the LOS projection of plate motion in the satellite far range from the projection in the satellite near range (see Figure 1, but note that the ramps in Figure 1 are plotted as a function of distance along the ground (ground range), not distance

October 9, 2022, 7:17pm

from the satellite (slant range)). These plots can be used for an estimate of the expected InSAR-derived velocity ramps given values of the plate motion velocity. Figure S6 shows that, for a given plate speed, the impact on the LOS velocity is largest when the plate is moving parallel to the heading angle of the LOS vector (i.e., approximately perpendicular to the satellite direction of motion). Note that in Figure S6 we use the line-of-sight vectors from the ascending and descending tracks over Aqaba (track 87 and track 21, respectively). While the pattern of LOS incidence angle variation across the track will be very similar for all tracks acquired in interferometric wideswath mode, the satellite orbit heading angle (and therefore the LOS heading angle) will vary with latitude due to the near-polar orbit of the Sentinel-1 satellites. The LOS heading angle also has a small variation across the track, which can be seen from the LOS geometry files (not shown here). Users should therefore examine the true LOS vector for their study area, and only use Figure S6 for a quick estimate of the ramps they could expect in their study regions.

Vertical secular bulk motion will have a different signature in ASC and DSC tracks compared to horizontal secular velocity. For horizontal plate motion to the east, for example, the ASC track will have a line of sight velocity gradient that is negative with increasing range and the descending track will have the opposite, assuming a right-looking satellite such as Sentinel-1 (Figure S6). When translated into geographic coordinates, this will result in both ASC and DSC tracks having negative velocity gradients to the east (Figure 1). In contrast, a constant, positive, vertical velocity will appear as negative LOS velocity gradients in range for ASC and DSC, which translates to a negative LOS velocity gradient to the east in the ASC track and a positive gradient to the east in the DSC track.

The gradients would be reversed for negative vertical velocities. This effect is illustrated in Figure 1(c), and we show examples of the ramp sizes for varying horizontal and vertical plate motion in Figure S6.

Altamimi et al. (2017) and Altamimi et al. (2012) have noted that plate motion models may be contaminated by the inclusion of stations undergoing glacial isostatic adjustment (GIA). Therefore it may not be appropriate to investigate GIA by subtracting a plate motion model from a velocity field, and a more careful investigation of the local velocity field might be warranted.

As suggested in the Conclusion, the signal of plate motion in InSAR data could be used to better constrain plate motion models. This could be limited to constraining horizontal plate motions, but if the direction of horizontal plate motion is known, then the velocity gradients of ascending and descending tracks combined could potentially be used to constrain the amplitude of horizontal and vertical plate motions together. Such constraints could prove useful for improving plate models, particularly where GNSS points are sparse. However, this approach could prove challenging if there were substantial contributions from noise sources and tectonic deformation, and would likely require long InSAR time series to reduce biasing of the velocity by non-secular terms, and long tracks to avoid biasing by short-wavelength velocity residuals.

Text S4: The Impact of Plate Motion on 3D Velocity Fields Derived from InSAR

While individual InSAR tracks only provide one line-of-sight for each point on the ground, multiple tracks with different LOS angles can be combined to constrain the 3D

October 9, 2022, 7:17pm

velocity field (Fialko et al., 2001; Wright et al., 2004). When an ascending and descending track covering the same region are available, these can be used to derive the horizontal and vertical velocities by assuming the direction of the horizontal velocity, and choosing the same reference point for both of these tracks, which is implicitly assumed to be stable in the reference frame of the satellite (e.g., Wright et al. (2004)). By assuming that this point is stable, we further assume that the ascending and descending track velocities can be explained purely by motions relative to this point, which means our solution cannot contain any overall translation. The assumption of a constant horizontal velocity direction also prohibits any rotational component in our inferred velocities in InSAR scenes. If there is in fact an overall translation or rotation of our observed region, this could lead to a biasing of our calculated horizontal and vertical velocities.

In Figure 4, we illustrate how plate motion biases our estimation of the 3D velocity field. We use the overlapping region of tracks 86 and 20 over the Makran subduction zone, and first apply the corrections show in Figures 2 and S1, (f)-(i), to each tracks 86 and 20, respectively. Using these two lines-of-sight we then calculate the horizontal and vertical velocities, assuming that horizontal velocity is purely due east. When we perform this calculation before plate motion correction, the east and vertical components contain long-wavelength velocity ramps (Figure 4 (a)-(b)). The vertical velocity has a ramp of around 3 mm/yr/100 km in the east-west direction, and the eastward velocity has a ramp of approximately 1.5 mm/yr/100 km in the north-south direction. These velocity ramps are primarily a bias from plate motion combined with the assumption that the reference point is fixed.

After removing the plate motion contribution to the ascending and descending tracks and repeating the calculation, the long-wavelength velocity ramps in the calculated horizontal and vertical maps are substantially reduced (Figure 4 (c)-(d)). There may be some remaining bias from the assumption that horizontal motion is purely east-west.

The bias from plate motion would not be present if the InSAR observations had had a ramp fitted and removed before the calculation (as is often done either with or without the help of GNSS), as this would remove the plate motion velocity ramp. The bias would also be less obvious if the area studied was smaller, or the tectonic signal was larger. The results in Figure 4 emphasize the importance of accounting for the reference frame of our observations before combining separate tracks.

References

Altamimi, Z., Métivier, L., & Collilieux, X. (2012). ITRF2008 plate motion model. *Journal of Geophysical Research: Solid Earth*, *117*(7), 1–14. doi: 10.1029/2011JB008930

Altamimi, Z., Métivier, L., Rebischung, P., Rouby, H., & Collilieux, X. (2017). ITRF2014 plate motion model. *Geophysical Journal International*, *209*(3), 1906–1912. doi: 10.1093/gji/ggx136

Ansari, H., De Zan, F., & Parizzi, A. (2021). Study of Systematic Bias in Measuring Surface Deformation with SAR Interferometry. *IEEE Transactions on Geoscience and Remote Sensing*, *59*(2), 1285–1301. doi: 10.1109/TGRS.2020.3003421

Bekaert, D., Walters, R., Wright, T., Hooper, A., & Parker, D. (2015). Statistical comparison of InSAR tropospheric correction techniques. *Remote Sensing of Environment*, *170*, 40–47. Retrieved from `https://linkinghub.elsevier.com/retrieve/pii/S0034425715301231` doi: 10.1016/j.rse.2015.08.035

Berardino, P., Fornaro, G., Lanari, R., & Sansosti, E. (2002). A new algorithm for surface deformation monitoring based on small baseline differential SAR interferograms. *IEEE Transactions on Geoscience and Remote Sensing*, *40*(11), 2375–2383. Retrieved from `http://ieeexplore.ieee.org/document/1166596/` doi: 10.1109/TGRS.2002.803792

Chen, C. W., & Zebker, H. A. (2002). Phase unwrapping for large SAR interferograms: Statistical segmentation and generalized network models. *IEEE Transactions on Geoscience and Remote Sensing*, *40*(8), 1709–1719. doi: 10.1109/TGRS.2002.802453

De Zan, F., Prats-Iraola, P., Scheiber, R., & Rucci, A. (2014). Interferometry with

TOPS: Coregistration and azimuth shifts. *Proceedings of the European Conference on Synthetic Aperture Radar, EUSAR*, *Proceeding*(0), 949–952.

Dicaprio, C. J., Simons, M., Kenner, S. J., & Williams, C. A. (2008). Post-seismic reloading and temporal clustering on a single fault. *Geophysical Journal International*, *172*(2), 581–592. doi: 10.1111/j.1365-246X.2007.03622.x

Emardson, T. R., Simons, M., & Webb, F. H. (2003). Neutral atmospheric delay in interferometric synthetic aperture radar applications: Statistical description and mitigation. *Journal of Geophysical Research: Solid Earth*, *108*(B5), 1–8. Retrieved from `http://doi.wiley.com/10.1029/2002JB001781` doi: 10.1029/2002JB001781

Fattahi, H., Agram, P., & Simons, M. (2017). A Network-Based Enhanced Spectral Diversity Approach for TOPS Time-Series Analysis. *IEEE Transactions on Geoscience and Remote Sensing*, *55*(2), 777–786. Retrieved from `http://ieeexplore.ieee.org/document/7637021/` doi: 10.1109/TGRS.2016.2614925

Fattahi, H., & Amelung, F. (2013). DEM Error Correction in InSAR Time Series. *Geoscience and Remote Sensing, IEEE Transactions on*, *51*(7), 4249–4259. Retrieved from `http://ieeexplore.ieee.org/document/6423275/` doi: 10.1109/TGRS.2012.2227761

Fattahi, H., & Amelung, F. (2014). InSAR uncertainty due to orbital errors. *Geophysical Journal International*, *199*(1), 549–560. doi: 10.1093/gji/ggu276

Fattahi, H., & Amelung, F. (2015). InSAR bias and uncertainty due to the systematic and stochastic tropospheric delay. *Journal of Geophysical Research: Solid Earth*, *120*(12), 8758–8773. Retrieved from `https://onlinelibrary.wiley.com/`

`doi/abs/10.1002/2015JB012419` doi: 10.1002/2015JB012419

Fattahi, H., Simons, M., & Agram, P. (2017). InSAR Time-Series Estimation of the
    Ionospheric Phase Delay: An Extension of the Split Range-Spectrum Technique.
    IEEE Transactions on Geoscience and Remote Sensing, *55*(10), 5984–5996. doi:
    10.1109/TGRS.2017.2718566

Fialko, Y., Simons, M., & Agnew, D. (2001). The complete (3-D) surface displacement
    field in the epicentral area of the 1999 Mw 7.1 Hector Mine earthquake, California,
    from space geodetic observations. *Geophysical Research Letters*, *28*(16), 3063–3066.
    doi: 10.1029/2001GL013174

Gomba, G., Parizzi, A., De Zan, F., Eineder, M., & Bamler, R. (2016). Toward opera-
    tional compensation of ionospheric effects in SAR interferograms: The split-spectrum
    method. *IEEE Transactions on Geoscience and Remote Sensing*, *54*(3), 1446–1461.
    doi: 10.1109/TGRS.2015.2481079

Hersbach, H., Bell, B., Berrisford, P., Hirahara, S., Horányi, A., Muñoz-Sabater, J.,
    ... Thépaut, J. (2020). The ERA5 global reanalysis. *Quarterly Journal of
    the Royal Meteorological Society*, *146*(730), 1999–2049. Retrieved from `https://`
    `onlinelibrary.wiley.com/doi/10.1002/qj.3803` doi: 10.1002/qj.3803

Jolivet, R., Agram, P. S., Lin, N. Y., Simons, M., Doin, M.-p., Peltzer, G., & Li, Z. (2014).
    Improving InSAR geodesy using Global Atmospheric Models. *Journal of Geophysical
    Research: Solid Earth*, *119*(3), 2324–2341. Retrieved from `https://onlinelibrary`
    `.wiley.com/doi/abs/10.1002/2013JB010588` doi: 10.1002/2013JB010588

Jolivet, R., Grandin, R., Lasserre, C., Doin, M. P., & Peltzer, G. (2011). Systematic

InSAR tropospheric phase delay corrections from global meteorological reanalysis data. *Geophysical Research Letters*, *38*(17), 1–6. doi: 10.1029/2011GL048757

Li, Z., Wright, T., Hooper, A., Crippa, P., Gonzalez, P., Walters, R., ... Parsons, B. (2016). Towards InSAR everywhere, all the time, with Sentinel-1. *International Archives of the Photogrammetry, Remote Sensing and Spatial Information Sciences - ISPRS Archives*, *41*(July), 763–766. doi: 10.5194/isprsarchives-XLI-B4-763-2016

Liang, C., Agram, P., Simons, M., & Fielding, E. J. (2019). Ionospheric Correction of InSAR Time Series Analysis of C-band Sentinel-1 TOPS Data. *IEEE Transactions on Geoscience and Remote Sensing*, *57*(9), 6755–6773. doi: 10.1109/tgrs.2019.2908494

Liang, C., Liu, Z., Fielding, E. J., & Bürgmann, R. (2018). InSAR time series analysis of L-Band wide-swath SAR data acquired by ALOS-2. *IEEE Transactions on Geoscience and Remote Sensing*, *56*(8), 4492–4506. doi: 10.1109/TGRS.2018.2821150

Milbert, D. (2018). *solid: Solid Earth Tide.* Retrieved from `https://geodesyworld` `.github.io/SOFTS/solid.htm`

Parizzi, A., Brcic, R., & De Zan, F. (2021). InSAR Performance for Large-Scale Deformation Measurement. *IEEE Transactions on Geoscience and Remote Sensing*, *59*(10), 8510–8520. doi: 10.1109/TGRS.2020.3039006

Petit, G., & Luzum, B. (2010). *IERS Conventions (IERS Technical Note No. 36).* Frankfurt, Germany. Retrieved from `http://www.iers.org/TN36/`

Rosen, P. A., Gurrola, E., Sacco, G. F., & Zebker, H. (2012). The InSAR scientific computing environment. In *Proceedings of the european conference on synthetic aperture radar, eusar* (Vol. 2012-April, pp. 730–733).

Wright, T. J., Parsons, B. E., & Lu, Z. (2004). Toward mapping surface deformation in three dimensions using InSAR. *Geophysical Research Letters*, *31*(1), 1–5. doi: 10.1029/2003GL018827

Xu, X., & Sandwell, D. T. (2020). Toward Absolute Phase Change Recovery with InSAR: Correcting for Earth Tides and Phase Unwrapping Ambiguities. *IEEE Transactions on Geoscience and Remote Sensing*, *58*(1), 726–733. doi: 10.1109/ TGRS.2019.2940207

Yu, C., Penna, N. T., & Li, Z. (2020). Ocean Tide Loading Effects on InSAR Observations Over Wide Regions. *Geophysical Research Letters*, *47*(15). doi: 10.1029/2020GL088184

Yunjun, Z., Fattahi, H., & Amelung, F. (2019). Small baseline InSAR time series analysis: Unwrapping error correction and noise reduction. *Computers and Geosciences*, *133*(May), 104331. Retrieved from `https://doi.org/10.1016/j.cageo .2019.104331` doi: 10.1016/j.cageo.2019.104331

Yunjun, Z., Fattahi, H., Pi, X., Rosen, P., Simons, M., Agram, P., & Aoki, Y. (2022). Range Geolocation Accuracy of C/L-band SAR and its Implications for Operational Stack Coregistration. *IEEE Transactions on Geoscience and Remote Sensing*, *2892*(c), 1–1. Retrieved from `https://ieeexplore.ieee.org/document/9759304/` doi: 10.1109/TGRS.2022.3168509

Zebker, H. A., & Villasenor, J. (1992). Decorrelation in interferometric radar echoes. *IEEE Transactions on Geoscience and Remote Sensing*, *30*(5), 950–959. doi: 10 .1109/36.175330

Zheng, Y., Fattahi, H., Agram, P., Simons, M., & Rosen, P. (2022). On Closure Phase and Systematic Bias in Multilooked SAR Interferometry. *IEEE Transactions on Geoscience and Remote Sensing*, *60*, 1–11. Retrieved from `https://ieeexplore` `.ieee.org/document/9758802/` doi: 10.1109/TGRS.2022.3167648

Table S1. Summary of Sentinel-1 SAR Data used. ASC: Ascending track. DSC: Descending track. Aqn. no.: Number of acquisitions. Makran and Aqaba use only Sentinel-1A data, Australia uses only Sentinel-1B. The plates used for plate motion corrections are listed in the final column and are taken from Table 1 of Altamimi et al. (2017).

Region	Track	Direction	Start date	End date	Aqn. no.	Plate
Makran	86	ASC	20141023	20210401	158	EURA
Makran	20	DSC	20141007	20210328	150	EURA
Aqaba	87	ASC	20141104	20220102	203	ARAB
Aqaba	21	DSC	20150815	20210503	160	ARAB
Australia	46	DSC	20161003	20211212	157	AUST
Australia	119	DSC	20160926	20211217	158	AUST

Table S2. Summary of spatial standard deviation σ (mm/year) among all the datasets in three different regions. The percentage in the parenthesis shows the percentage of σ reduction compared with the σ from its' previous stage. Negative percentage means σ decreases. Numbers are plotted in Figure 2k.

Track	Raw	-Ion	-Ion -ERA5	-Ion -ERA5 -SET	-Ion -ERA5 -SET -Topo	-Ion -ERA5 -SET -Topo -PMM
a087	6.090	2.872 (-52.8%)	2.529 (-11.9%)	2.515 (-0.6%)	2.508 (-0.3%)	1.532 (-38.9%)
d021	2.971	2.793 (-6.0%)	2.646 (-5.3%)	2.629 (-0.6%)	2.629 (-0.0%)	2.046 (-22.2%)
a086	8.304	2.015 (-75.7%)	2.071 (2.8%)	2.082 (0.5%)	2.064 (-0.8%)	1.230 (-40.4%)
d020	2.030	2.334 (15.0%)	2.155 (-7.7%)	2.118 (-1.7%)	2.124 (0.3%)	1.224 (-42.4%)
d119	2.796	2.801 (0.2%)	2.161 (-22.8%)	2.131 (-1.4%)	2.131 (0.0%)	1.753 (-17.7%)
d046	2.250	2.266 (0.7%)	2.202 (-2.8%)	2.187 (-0.7%)	2.195 (0.4%)	1.594 (-27.4%)

Table S3.   Summary of spatial standard deviation σ (mm/year) of each correction among all the datasets in three different regions. Numbers are plotted in Figure S7.

Track	Ion	ERA5	SET	Topo	PMM
a087	3.569	0.863	0.048	0.052	1.957
d021	0.923	0.867	0.056	0.013	1.531
a086	7.147	0.921	0.086	0.098	1.663
d020	0.470	0.619	0.064	0.039	1.545
d119	0.316	1.547	0.189	0.019	1.162
d046	0.400	0.641	0.061	0.045	1.141
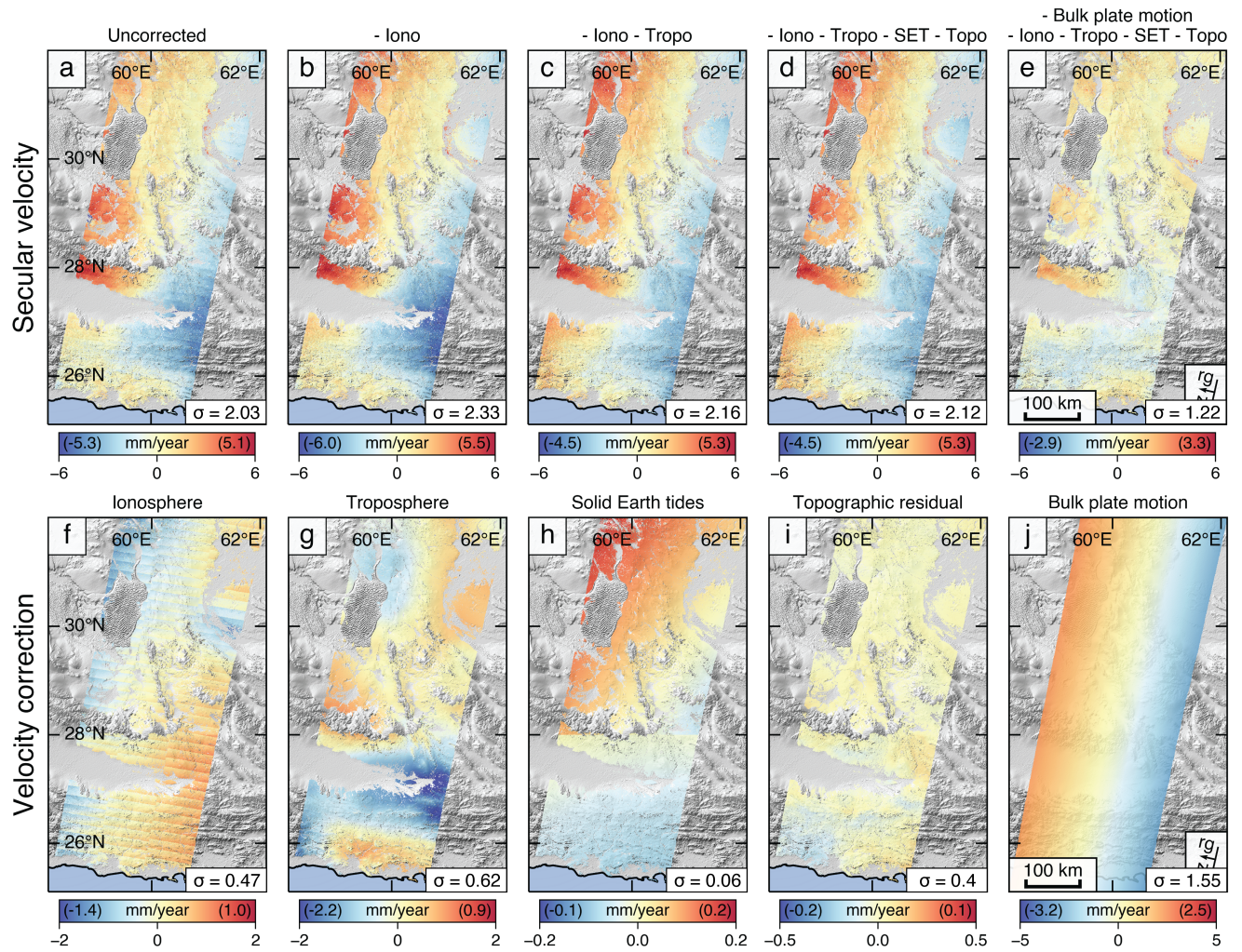
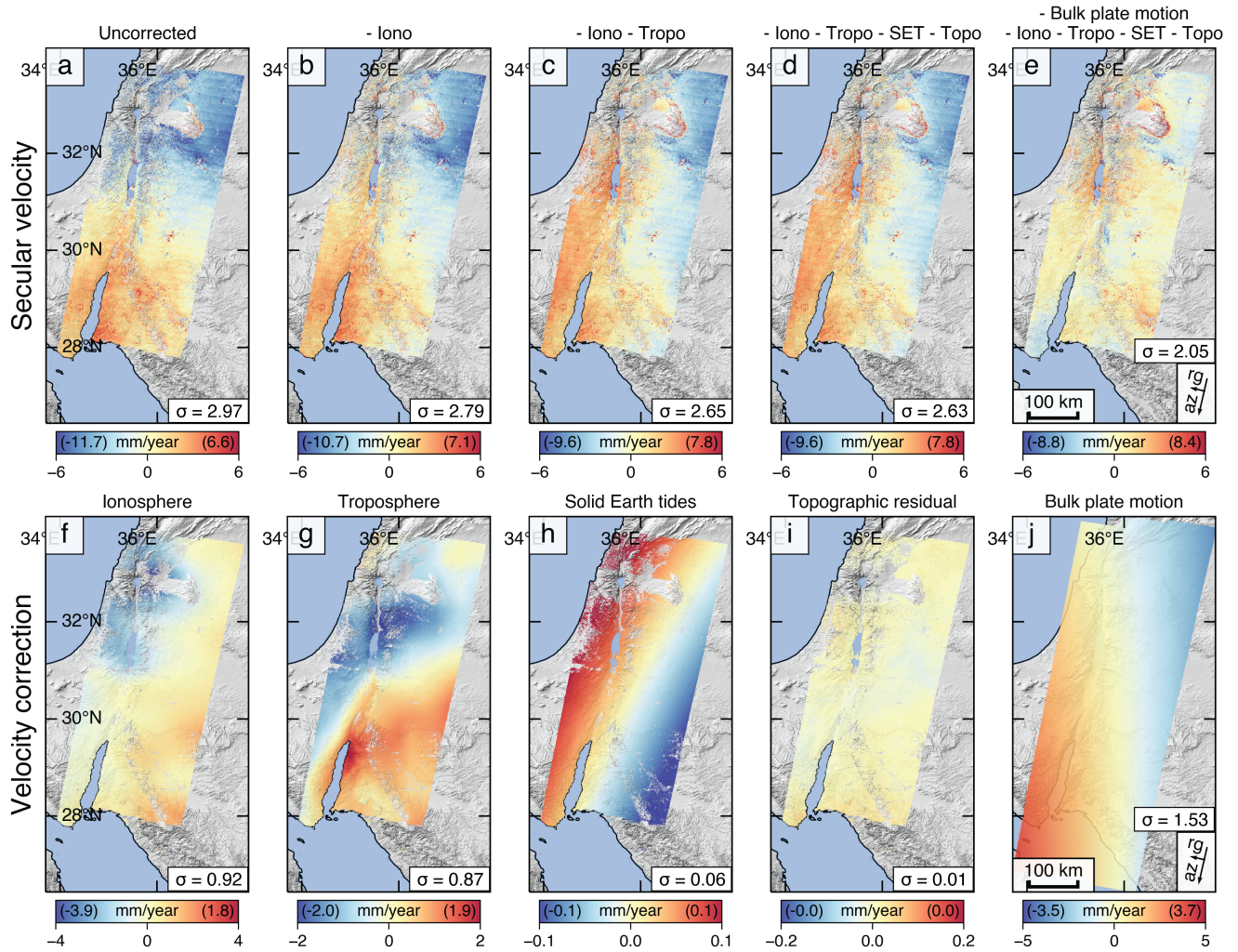**Figure S1.** Cumulative impact of corrections on the InSAR-derived velocity field for Sentinel-1, track 20 (DSC) over the Makran subduction zone. Panels are as described in Figure 2. Note the substantial difference in the long-wavelength ionospheric correction between ASC (Figure 2(f)) and DSC tracks ((f)). The burst discontinuities due to the ionosphere can be clearly seen in (f) (Liang et al., 2019). σ is each panel corresponds to the spatial standard deviation of the velocity field (mm/year) as defined in the main text.

October 9, 2022, 7:17pm
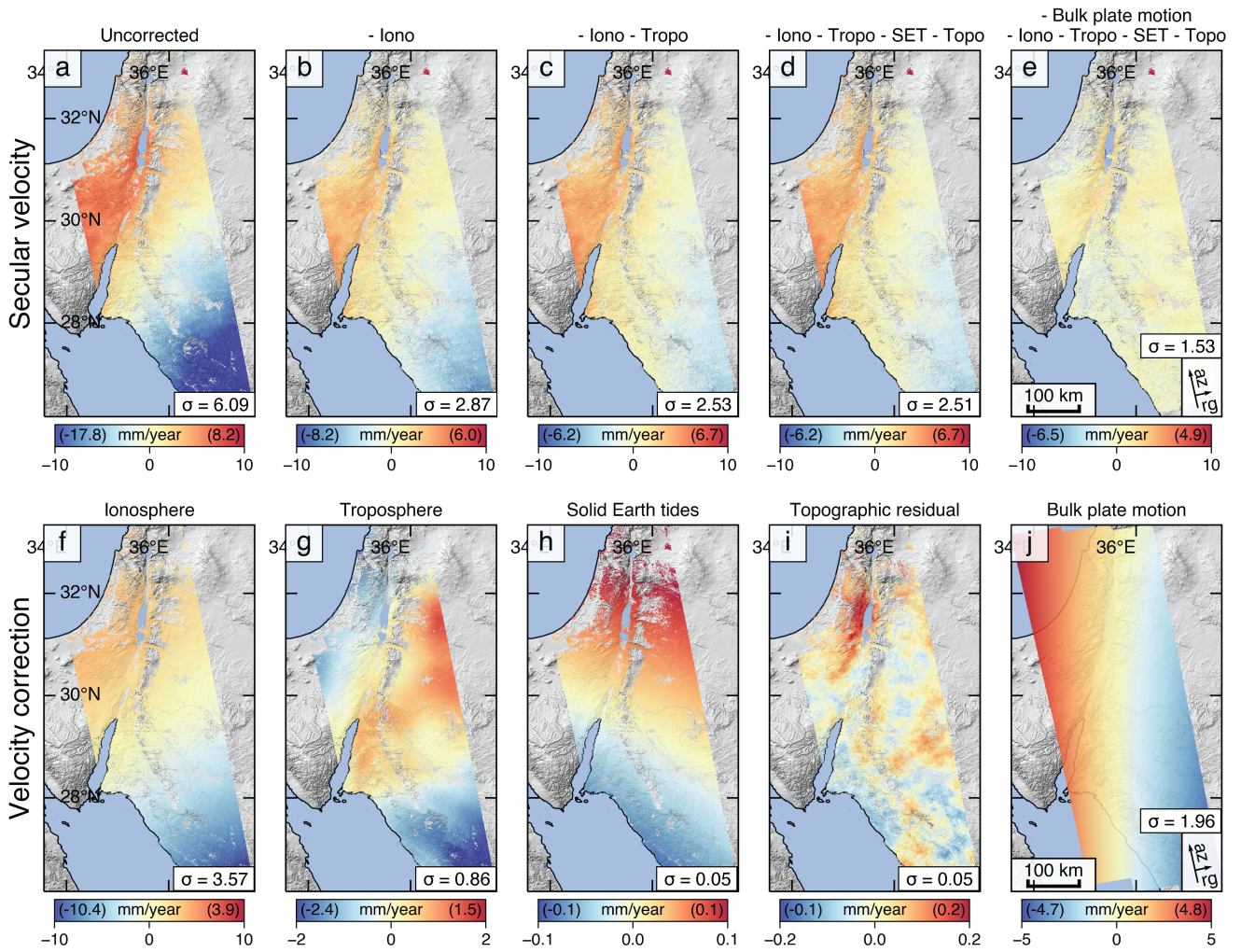
Figure S2.   Cumulative impact of corrections on the InSAR-derived velocity field for Sentinel-1, track 87 (ASC) over the Gulf of Aqaba. Panels are as described in Figure 2.

Figure S3. Cumulative impact of corrections on the InSAR-derived velocity field for Sentinel-1, track 21 (DSC) over the Gulf of Aqaba. Panels are as described in Figure 2.
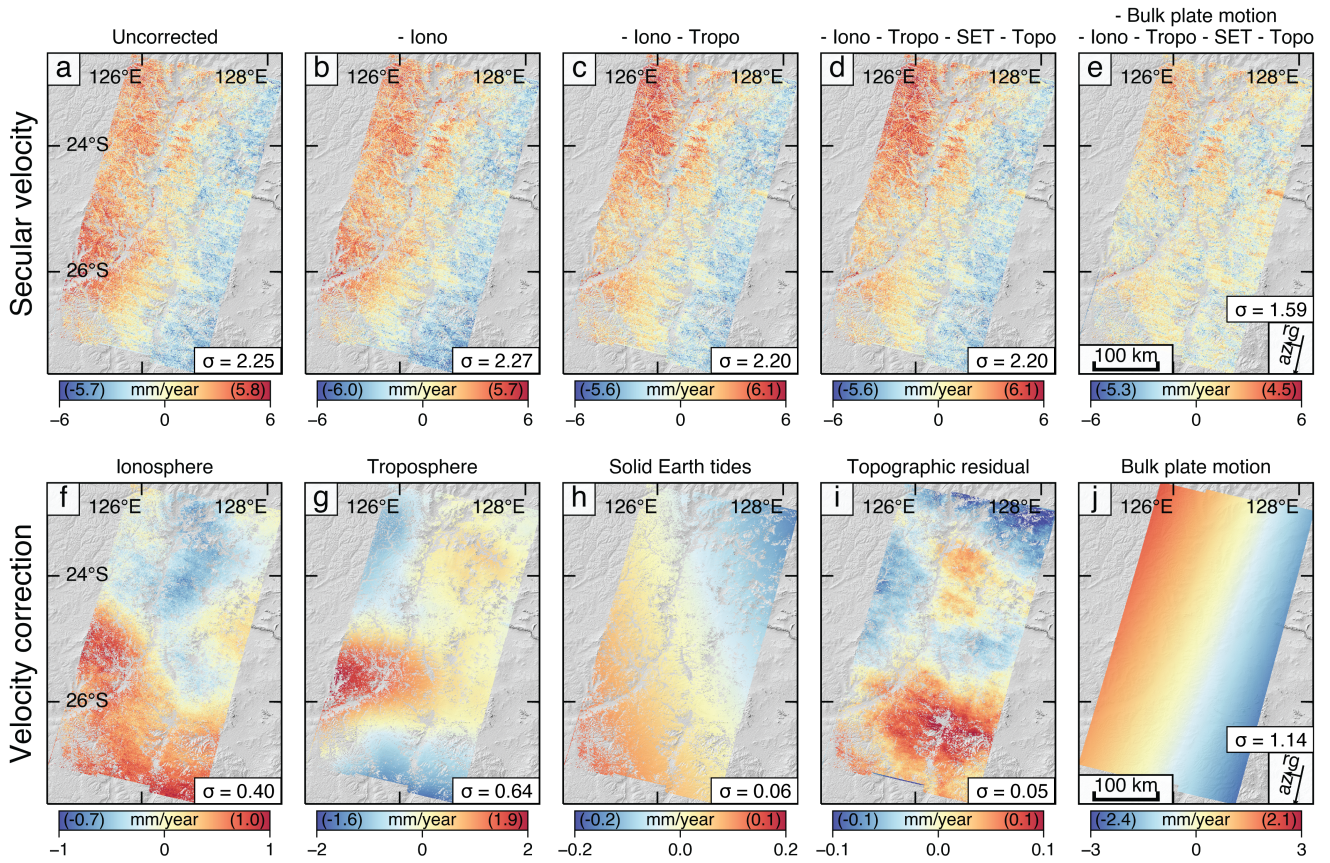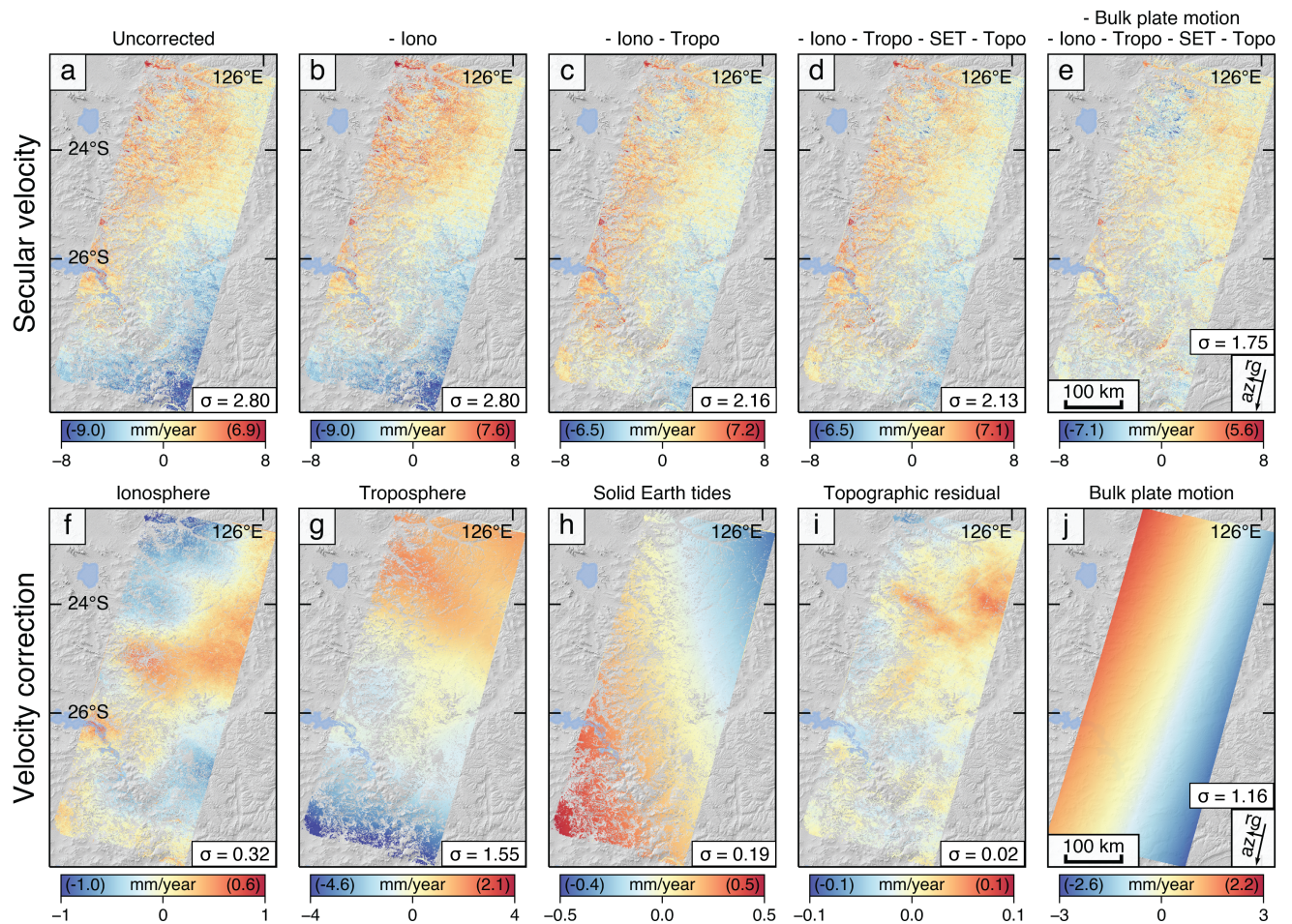
October 9, 2022, 7:17pm

Figure S4. Cumulative impact of corrections on the InSAR-derived velocity field for Sentinel-1, track 46 (DSC) over western Australia. Panels are as described in Figure 2.

Figure S5. Cumulative impact of corrections on the InSAR-derived velocity field for Sentinel-1, track 119 (DSC) over western Australia. Panels are as described in Figure 2.
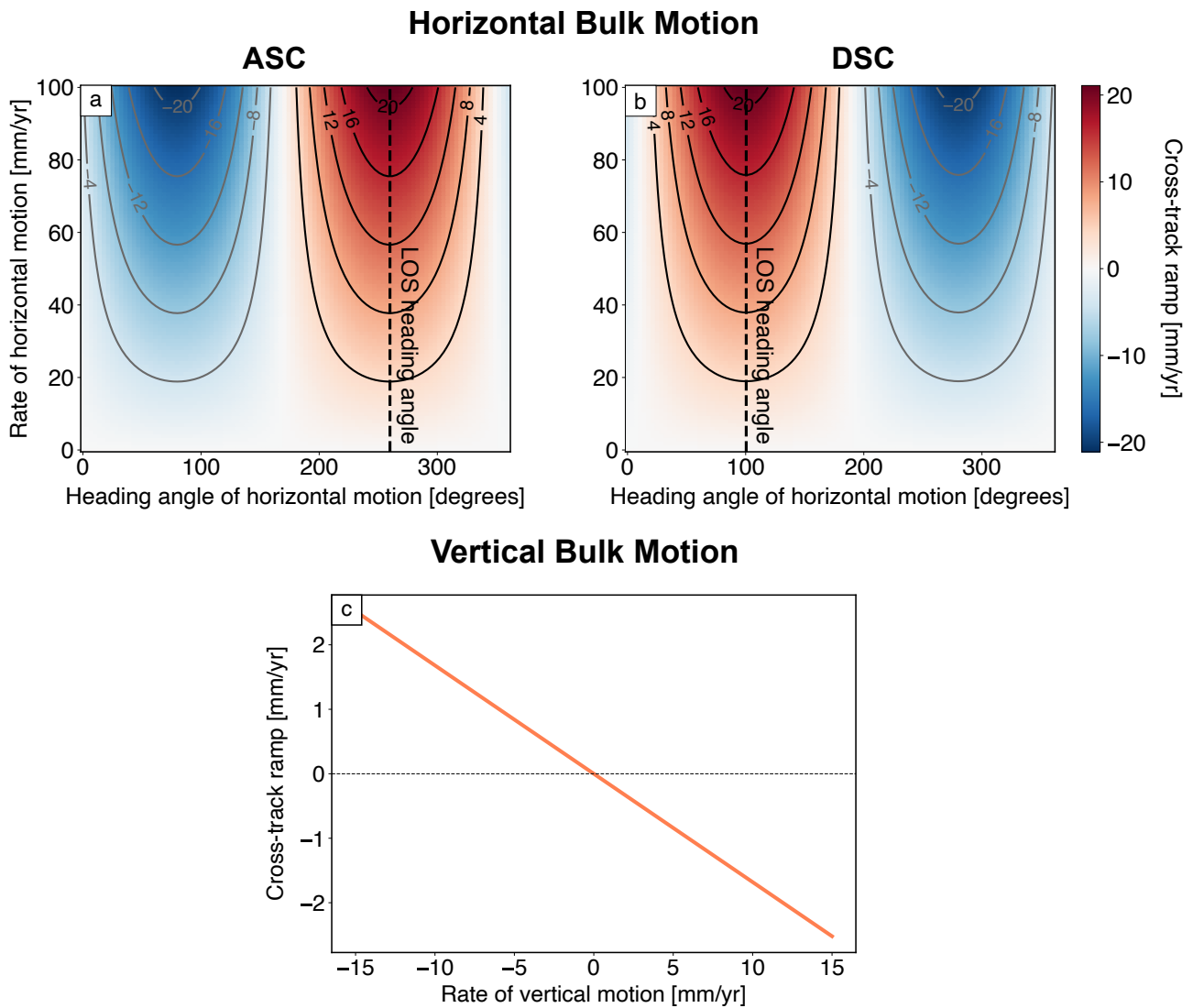
Horizontal Bulk Motion

Vertical Bulk Motion

Figure S6.   Size of velocity ramp in range for the 250 km wide Sentinel-1 swath for varying horizontal and vertical bulk motion. These calculations assume a constant plate velocity (i.e., no rotation), ignore the slight curvature in the across-track ramps (Figure 1), and take the LOS geometry from the ASC and DSC Sentinel-1 tracks over Aqaba (87 and 21, respectively). The LOS vector points from the ground to the satellite. Heading angles are measured clockwise from north. "LOS heading angle" is the heading angle of the horizontal projection of the LOS vector. "Heading angle of horizontal motion" is the heading angle of the bulk plate motion. A positive cross-track ramp means that LOS velocity increases with increasing satellite range. **(a)** Size of velocity ramp for horizontal motion in an ASC track. **(b)** Size of velocity ramp for horizontal motion in a DSC track. **(c)** Size of velocity ramp for vertical velocity motion. For vertical motion, the ramp has the same variation with range for ASC and DSC tracks.
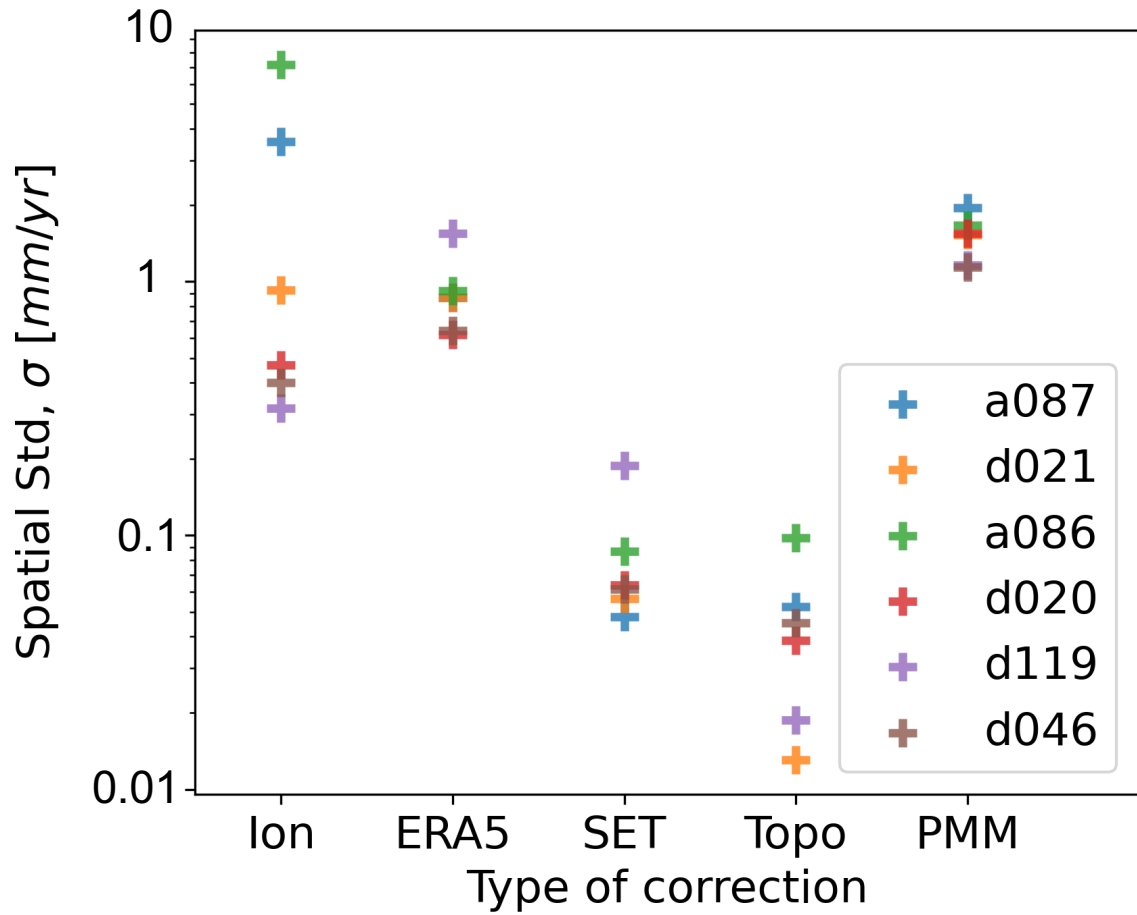
October 9, 2022, 7:17pm

Figure S7. The spatial standard deviation σ computed from each correction screen of the LOS velocity. Numbers are referenced to Table S3.
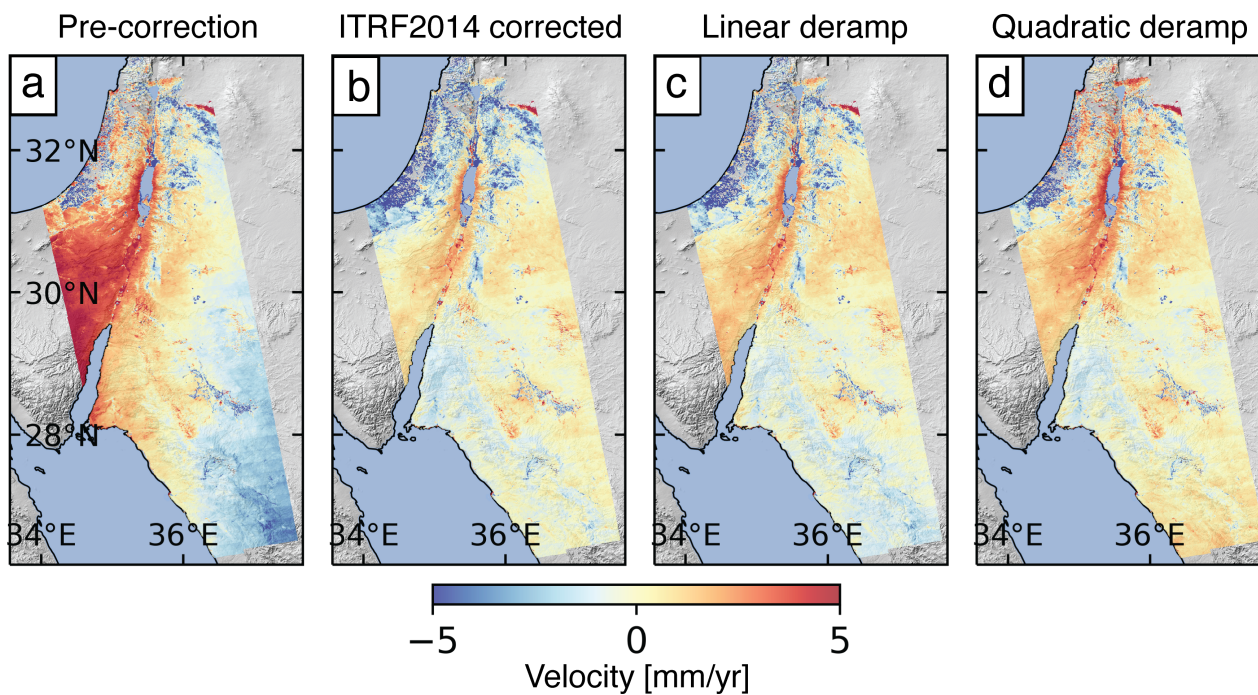
Figure S8.   The comparison between plate motion correction with quadratic empirical deramp-ing in the Aqaba region. (a) Without PMM correction. (b) With ITRF2014 PMM correction. (c) Remove a linear ramp in latitude and longitude directions. (d) Remove a quadratic ramp in latitude and longitude directions. These results show how empirical deramping can result in biases in the final velocity field compared to PMM corrections.

October 9, 2022, 7:17pm